ChemPhysChem

Research Article
doi.org/10.1002/cphc.202400272

Chemistry Europe
European Chemical Societies Publishing

www.chemphyschem.org

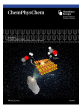

Formation of Methanol via Fischer-Tropsch Catalysis by Cosmic Iron Sulphide

Berta Martinez-Bachs,[a] Alexia Anguera-Gonzalez,[a] Gerard Pareras,*[a] and Albert Rimola*[a]

Chemical reactions in the gas phase of the interstellar medium face significant challenges due to its extreme conditions (i.e., low gas densities and temperatures), necessitating the presence of dust grains to facilitate the synthesis of molecules inaccessible in the gas phase. While interstellar grains are known to enhance encounter rates and dissipate energy from exothermic reactions, their potential as chemical catalysts remain less explored. Here, we present mechanistic insights into the Fischer-Tropsch-type methanol (FTT-CH_3OH) synthesis by reactivity of CO with H_2 and using cosmic FeS surfaces as heterogeneous catalysts. Periodic quantum chemical calculations were employed to characterize the potential energy surface of the reactions on the (011) and (001) FeS surfaces, considering different Fe coordination environments and S vacancies. Kinetic calculations were also conducted to assess catalytic capacity and allocate reaction processes within the astrochemical framework. Our findings demonstrate the feasibility of FeS-based astrocatalysis in the FTT-CH_3OH synthesis. The reactions and their energetics were elucidated from a mechanistic standpoint. Kinetic analysis demonstrates the temperature dependency of the simulated processes, underscoring the compulsory need of energy sources considering the astrophysical scenario. Our results provide insights into the presence of CH_3OH in diverse regions where current models struggle to explain its observational quantity.

Introduction

The history of our Solar System begins within a cold ($T \approx 5$–10 K) and dense ($n \approx 10^4$–10^5 H/cm^3) molecular cloud clump known as the Solar Nebula. Over the course of approximately 4.5 billion years, this nebula evolved into the planetary system we know today. In our local galaxy, the Milky way, there are thousands of Solar-like forming planetary systems at different stages. Their formation takes place through five different steps: the prestellar, the protostellar, the protoplanetary disk, the planetesimal, and the planet formation phases. The physical conditions are different among the phases; for instance, while in the prestellar phase the cold molecular clouds reside, protoplanetary environments available in later stages are warmer and denser. Moreover, from the chemical standpoint, there is a progression in chemical complexity alongside the steps, in which more complex molecules form at each step.[1,2] Indeed, observations spanning from radio to near-infrared wavelengths detect rovibrational transitions of almost 300 different gas-phase molecular species in different astrophysical environments, reflecting the rich chemical diversity and complexity in space.[3] The discovery of complex organic molecules within the interstellar medium (ISM) changed our understanding of our astrochemical origin, reinforcing the hypothesis that the basis of terrestrial life can have an extraterrestrial origin.[4–6] Interstellar complex organic molecules[7–9] (iCOMs) enjoy a central position in this ladder of organisational chemical transformation linked to a star and planetary formation. Indeed, despite being relatively small according to terrestrial chemical standards (typically ranging from 6 to 12 atoms), iCOMs are C-bearing species (alongside H, O and N, e.g., formamide (NH_2CHO)[10]), representing the dawn of the organic chemistry.[11,12] Moreover, chemical reactions involving iCOMs lead to the formation of molecules of enhanced complexity, some of them of prebiotic interest such as amino acids, fatty acids, sugars, and nucleobases, which are the biomolecular building blocks for terrestrial life.[13–16]

The increasing chemical complexity during the evolution of Solar-like planetary systems establishes a clear link between iCOMs and the origin of life. However, the specific chemical processes governing the formation and reactivity of iCOMs remain a critical and unresolved issue.[1,14,15,17,18] Understanding the formation of these species represents one of the most active research areas in Astrochemistry. The different pathways for both the formation and destruction of iCOMs are still subject of a vivid debate,[17–21] with new approaches[22] emerging to shed some light in this topic. One prevailing paradigms for the synthesis of iCOMs is the gas-phase scenario, where they are indeed observed. However, not all the molecules can be formed by gas-phase reactions in abundances consistent with observations. Therefore, the participation of dust grains (i.e., submicron-sized solid-state particles ubiquitously present in space) in the reactions is advocated. For instance, H_2 formation, the simplest but the most abundant molecule in the Universe, is

---

[a] *B. Martinez-Bachs, A. Anguera-Gonzalez, G. Pareras, A. Rimola*
Departament de Química, Universitat Autònoma de Barcelona, 08193
Bellaterra, Catalonia, Spain
E-mail: albert.rimola@uab.cat
gerard.pareras@uab.cat

Supporting information for this article is available on the WWW under https://doi.org/10.1002/cphc.202400272

only explained if it occurs on the surfaces of dust grains.[23–28] The increasing chemical complexity during the evolution of Solar-like planetary systems establishes a clear link between iCOMs and the origin of life. However, the specific chemical processes governing the formation and reactivity of iCOMs remain a critical and unresolved issue.[1,14,15,17,18] Understanding the formation of these species represents one of the most active research areas in Astrochemistry. The different pathways for both the formation and destruction of iCOMs are still subject of a vivid debate,[17–21] with new approaches[22] emerging to shed some light in this topic. One prevailing paradigms for the synthesis of iCOMs is the gas-phase scenario, where they are indeed observed. However, not all the molecules can be formed by gas-phase reactions in abundances consistent with observations. Therefore, the participation of dust grains (i.e., submicron-sized solid-state particles ubiquitously present in space) in the reactions is advocated. For instance, formation H_2, the simplest but the most abundant molecule in the Universe, is only explained if it occurs on the surfaces of dust grains.[23–28]

Dust grains form as a result of the ejection of gas and dust by a dying old star (namely, in the very first stage in the planetary system formation), which subsequently undergoes gravitational aggregation forming interstellar diffuse clouds ($T \approx 50–100$ K and gas density $n \approx 10–10^2$ H/cm^3). At this stage, dust grains consist of bare silicates and carbonaceous material, while the gaseous component is mainly in the form of atoms and simple diatomic species. Although relatively simple, the interstellar chemistry begins here. Moreover, interstellar grains are ubiquitous across the different astrophysical evolutionary stages. They initially exist as bare particles, then become covered by ices (in the prestellar and protoplanetary phases), ultimately coagulating into larger bodies (in the planetesimals phase), as the seeds of planets, comets, meteorites and other asteroidal bodies. From a chemical standpoint, they serve as solid-state supports for chemical reactions occurring in the ISM. Moreover, recent studies indicate that due to their porous and inhomogeneous surfaces, when dust grains are covered in ices, the refractory cores are still partially exposed to the surrounding gas environment.[29]

As mentioned above, the refractory part of the grains (namely, that not constituted by the volatile ices) can consist of Mg/Fe-silicates, prevalently in the amorphous structural state.[29–31] Due to the very low gas density, grain surface chemistry adopts Langmuir–Hinshelwood mechanisms. Interstellar grains facilitate that chemical reactions occur on their surfaces, serving mostly as reactant concentrators, third bodies, and chemical catalysts. However, there is limited evidence on the chemical catalytic properties of grains, advocated to provide alternative pathways with lower activation energy barriers. Indeed, comprehensive investigations into proper interstellar catalytic processes remain largely unexplored, primarily because most studies focus on ices, whose capability to reduce activation barriers is rather limited.[32] Nevertheless, beyond ices, there are other materials that may exhibit catalytic properties. Transition metals are present in the ISM, being iron particularly abundant, either incorporated into the grain structure as Fe-containing silicates or deposited onto grain surfaces as single atoms or clusters, thus forming potential astrocatalytic systems.[33,34]

The presence of iron in the ISM has been largely discussed due to its significant abundance compared to the other transition metals. Indeed, the depletion of iron from the gas phase into dust is particularly prominent in the ISM.[35–37] One possibility is that iron is included in the silicate structure of grains, although the observed interstellar silicates are largely magnesium-rich. Alternatively, iron may exist in its metallic form and also in the form of iron sulphide (FeS), which are frequently identified as inclusions in comets and meteorites,[38–45] (formed during the planetesimal phase) in which, interestingly, both Fe-bearing systems possess potential catalytic properties to take place in astrophysical environments. In the case of FeS, despite being important solid reservoirs of the cosmic sulphur and iron elements, their chemical behaviour in space-exposed environments is poorly understood.

FeS grains have been found as refractory materials in the protoplanetary disks around young stellar objects[42] and also in meteoritic samples as inclusions in glass with embedded metal and sulphides.[40,46] The presence of FeS inclusions in comets, which are considered primitive pre-solar bodies and hence reservoirs of volatile and refractory material formed in early stages, suggests that FeS have been conserved and inherited within dust grains throughout various stages of Solar-like planetary system formation. The existence of these FeS inclusions in grains provides thus opportunities for true astrocatalysis, acting as catalytic active sites. Research on astrocatalysis is a growing field in Astrochemistry but still in its infancy, resulting in limited literature. Recent studies have primarily focused on Fischer-Tropsch-type (FTT) reactions for the formation of alcohols and short-chain alkenes. Laboratory experiments have successfully synthesized hydrocarbons using transition metal-containing dust analogues under solar nebula conditions.[47–50] Additionally, a recent computational study by some of us indicates the feasibility of methanol formation within the ISM catalysed by Fe single-atoms supported on silica, although requiring a minimum amount of energy to trigger the mechanism.[51] FTT reactions have been object of study in astrochemistry due to the abundance of the H_2 and CO reactants (the first and second most abundant gas-phase molecules in the ISM) and their exothermic nature, compulsory conditions for astrochemical reactions due to the very low temperatures and pressures. Other investigations dedicated to elucidate astrocatalysis point out that cometary grains can indeed selectively catalyse the formation of relevant prebiotic molecules, the catalytic properties of which are due to the heterogeneity of their structures.[52–55] Although the positive assessment about the occurrence of catalytic processes on cosmic grains, there is a lack of comprehensive studies regarding the catalytic mechanisms of these reactions and the identification of potential active catalysts that can trigger such processes.

In the present study, we investigate the formation of methanol (CH_3OH) through the simplest FTT reaction (one CO molecule and two H_2 molecules) catalysed by FeS surfaces (see the scheme of Figure 1). The reaction mechanisms have been

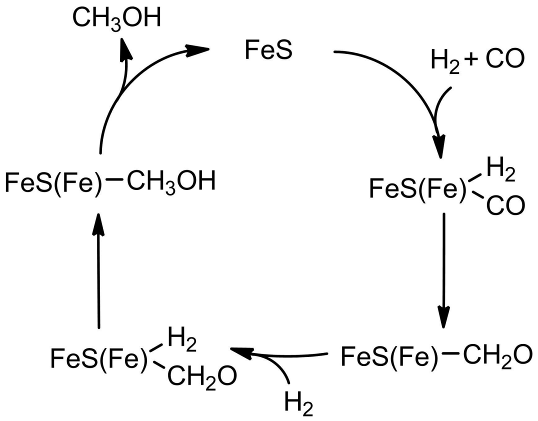

Figure 1. Proposed catalytic cycle for the formation of methanol (CH$_3$OH) from the reactivity of CO with two H$_2$ molecules catalysed by a FeS surface. The Fe in parenthesis denotes that atom involved in the chemical reactions.

elucidated by characterising their potential energy surfaces, and kinetic calculations have been performed to assess the catalytic capabilities of FeS within an astrochemistry context. The aim of this work is to exploit the versatility of FeS (present in different stages of a planetary system formation) as catalytic materials to enhance our understanding on the chemical evolution beyond the cold and early stages of Solar system formation, where the ice chemistry predominates.

Methods

Computational Details

The surface catalysts were modelled using a periodic approach (further details regarding their modelling and structure are provided below). Quantum chemical calculations were performed with the CP2K package.[56] The characterization of the potential energy surface (PES) of the reactions requires determining the structures and the energetics of the stationary points. For geometry optimizations, the semi-local PBEsol functional was used,[57] along with the Grimme D3(BJ) correction to include dispersion forces.[58] A double-ζ basis set (DZVP-MOLOPT-SR-GTH gaussian basis set) was adopted for all the atom types, combined with a cut-off set at 500 Ry for the plane wave auxiliary basis set.[59,60] The Goedecker–Teter–Hutter pseudopotentials[61] were used to describe core electrons, while a mixed Gaussian and plane-wave (GPW) approach[62] was employed for valence electrons. The energies of the stationary points were refined by performing single point calculations onto PBEsol-optimized geometries employing the hybrid B3LYP functional,[63,64] with the D3(BJ) dispersion correction and using the triple-ζ basis set (TZVP). This B3LYP-D3(BJ)//PBEsol-D3(BJ) scheme is a very cost-effective for the investigated systems and reactions, giving rise to accurate results (PBEsol-D3(BJ) for geometry optimizations performances and B3LYP–D3(BJ) for the energetics) at a reasonable computational cost. Note that the auxiliary density matrix method (ADMM)[65,66] was used for the Hartree-Fock exchange when performing calculations with hybrid functionals.

The climbing image nudged elastic band (CI-NEB) technique implemented in CP2K[56] was used to search for transition states. The CI-NEB calculations were run at PBEsol-D3(BJ) and then, onto the identified transition states, single point calculations at B3LYP-D3(BJ) were performed to refine the energetics. Energy barriers were calculated as:

$$\Delta E^{+} = E_{TS} - E_{GS} \tag{1}$$

$$\Delta U^{+} = \Delta E^{+} - \Delta ZPE \tag{2}$$

$$\Delta G_T^{\ddagger} = \Delta E^{+} + \Delta G_T \tag{3}$$

where ΔE^{+} stands for the potential energy barrier, and E_{TS} and E_{GS} for the absolute potential energies of the transition states and the previous local minima, respectively. ΔU^{+} represents the zero-point energy (ZPE) corrected barrier (in which ΔZPE refers to the contribution of the ZPE corrections to ΔE^{+}), and $\Delta G_T^{\ddagger}$ for the Gibbs activation barrier at a given temperature (in which ΔG_T refers to the contribution of the Gibbs corrections to ΔE^{+}).

Binding energies of the reactants, products and reaction intermediates were computed through the counterpoise method, implemented in CP2K, to subtract basis set superposition error (BSSE). Final binding energies were calculated as:

$$\Delta E_{ads} = E_{cplx} - (E_{sur} - E_m) \tag{4}$$

$$\Delta U_{ads} = \Delta E_{ads} + \Delta ZPE \tag{5}$$

$$BE = -\Delta U_{ads} \tag{6}$$

where ΔE_{ads} denotes the adsorption potential energy, and E_{cplx}, E_{sur} and E_m the absolute potential energies for the adsorption complex, the isolated surface, and the isolated molecule, respectively. ΔU_{ads} is the ZPE-corrected adsorption energy, where ΔZPE accounts for the contribution of the ZPE correction to ΔE_{ads}, and BE is the binding energy, which equals ΔU_{ads} with opposite sign.

The nature of the stationary points of the reactions was validated by calculating the harmonic frequencies; the outcome being minima for reactants, intermediates and products, and first-order saddle points for transitions states. Vibrational harmonic frequencies were calculated at the PBEsol-D3BJ/DZVP-optimized structures using the finite differences method as implemented in the CP2K code.[59] To minimize the computational cost, a partial Hessian approach was employed. Consequently, vibrational frequencies were computed solely for a subset of the entire system, comprising the surface atoms participating in the reaction and the reactive species.

The catalytic performance of the simulated FTT processes was investigated with kinetic calculations. The rate constants for each elementary barrier were computed using the Rice–Ramsperger–Kassel–Marcus (RRKM) theory,[67] which were implemented in a freely available home-made program to obtain rate constants for surface reactions.[68] RRKM is a microcanonical transition state theory that assumes that the phase space is statistically populated. For a reaction step with an energy barrier E_0, the microcanonical rate constant $k(E)$ at a given total energy E (where $E > E_0$) is expressed as:

$$k(E) = \frac{N^{\neq}(E - E_0)}{h\rho(E)} = \frac{\int_0^{E_0} T\left(\xi^{\neq}\right) d\xi^{\neq} \int_0^{E-E_0} \rho^{\neq}(E - E_0 - \xi^{\neq}) d\xi^{\neq}}{h\rho(E)} \tag{7}$$

where $N^{\neq}(E - E_0)$ represents the sum of states for the TS with energies ranging from 0 to $E - E_0$, $\rho(E)$ is the density of states of reactants (i.e., the number of states per unit of energy, in quantum mechanics this refers to the degeneracy $g(E)$), and h the Planck constant. The sum of states of the TS can be integrated over the translational energy of the reaction coordinate $\xi^{\neq}$, where tunnelling effects are considered through the transmission probability $T(\xi^{\neq})$ within the integral, with the integration range extending from 0 to E_0. The microcanonical $k(E)$ can then be converted to canonical $k(T)$ by distributing energy levels according to the Boltzmann distribution:

$$(T) = \int_{E_0}^{\infty} k(E)xP(E)dE = \int_{E_0}^{\infty} k(E)x\frac{g(E)\exp(-E/k_BT)}{Q(T)}dE \tag{8}$$

where $Q(T)$ is the total partition function. Analytical expressions for $T(\xi^{\neq})$ can be obtained using specific potential barrier shapes; in this study, the unsymmetrical Eckart potential barrier[69] was employed due to its proven accuracy in accounting for tunnelling in reactions of astrochemical interest.[70]

Finally, the rate constants were represented in the form of Arrhenius plots (i.e., $\ln[k(T)]$ *vs* $1/T$), where the temperature effect on the rate constants is given by:

$$\ln[k(T)] = \ln(A) - \frac{E_a}{R}\left(\frac{1}{T}\right) \tag{9}$$

where E_a denotes the activation energy, A is the pre-exponential factor, R is the ideal gas constant, and T is the temperature. A change in slope of the Arrhenius plot indicates the dominance of tunnelling.[51]

FeS Surface Models

Cosmic iron sulphides have been found to be in the form of troilite (FeS with 1:1 ratio) and pyrrhotite ($Fe_{(1\text{-}x)}S$, x = 0 to 0.17, depending on the number of Fe vacancies). Both forms typically occur in association with other minerals in meteorites, providing valuable insights into the formation and evolution of these celestial bodies and, by extension, about the processes that occurred in the early solar system. In this work, since we model the surfaces within periodic boundary conditions (in which keeping the electroneutrality of the solid surfaces is a compulsory constraint) we adopted troilite as the cosmic FeS system.

The bulk of FeS troilite exhibits a hexagonal structure (space group $P\bar{6}2c$), with X-ray diffraction crystallographic cell parameters of a = b = 5.896 Å and c = 11.421 Å, and α = β = 90 degrees and γ = 120 degrees, which upon PBEsol optimization convert into a = 5.697 b = 5.580 Å and c = 10.208 Å, and α = β = 90 degrees and γ = 120 degrees. Different slabs (see Table 1) were generated from the optimized bulk using the POLYCLEAVER code, a freely available home-made program developed in our group to generate stoichiometric and non-polar surface slab models of complex solid-state systems (e.g., ionic surfaces with polyatomic anions, e.g., silicates).[71] Note that the original unit cell of the Bulk structure has 24 atoms, but in order to build the different slabs we used a super cell of 96 atoms. The generated surfaces were then optimized, and respective surface energies (*Y*) calculated (values reported in Table 1) following the equation of

$$\Upsilon = \frac{E_{slab}^{relaxed} - nE_{bulk}}{2A} \tag{10}$$

where $E_{slab}^{relaxed}$ represents the energy of the optimized slab model, E_{bulk} the energy of the original optimized bulk structure, n the number of bulk FeS units present in the slab model, and A the slab surface area.

The calculated surface energies indicate that the most and least stable surfaces correspond to the (011) (001) slab models, respectively. For the (011) surface, Fe atoms can be either penta-coordinated or tetra-coordinated (see Figure 2), offering two distinct active sites (hereafter referred to as Penta-Fe@$FeS_{(011)}$ and Tetra-Fe@$FeS_{(011)}$, respectively). In the case of the (001) surface, Fe atoms are solely tri-coordinated, hereafter referred to as Tri-Fe@$FeS_{(001)}$ In addition to these surfaces, a defective structure from the (011) slab was also considered. Note that differently than in heterogeneous catalysis on Earth, the formation of defects is not related to the effect of the H_2 and CO on the surface,[72] as astrophysical environments present extreme conditions of low temperatures, pressures and molecular densities compared to terrestrial standards. Matter of fact, surface defects in grains are caused by processing of the grains due to the harsh-physical conditions of the environments. Examples of this processing are space weathering and sputtering of the grains due to stellar shock waves. This defective structure was generated by removing a S atom to create a sulphur vacancy. To maintain the stoichiometry (and hence the electroneutrality), a Fe atom was removed from the opposite face of the slab (see Figure 2). After optimizing this defective surface (hereafter referred to as Def-$FeS_{(011)}$), contraction and expansion of the Fe–Fe bond distances (Fe–Fe = 2.75 Å and Fe–Fe = 3.62 Å) is observed in the vicinity of the sulphur vacancy compared to the average distance in the non-defective (011) slab (Fe–Fe = 3.30 Å). The loss of coordination in surface Fe atoms contributes to the instability of the slabs, but from a catalysis perspective this could result in more reactive sites, and accordingly enhanced catalytic properties. Therefore, simulations were performed on these potential catalytic sites the penta-, tetra-, tri-coordinated surface Fe atoms and the defective surface.

Table 1. Collected the different Miller indices considered in this work and, their respective surface areas in Angstroms (Å), calculated surface energies (ϒ) in (J m^{-2}), the *n* values, optimized cell parameters in (Å) and the thickness of the slab in (Å).

Miller indices	Surface Area	ϒ	*n*	Cell Parameters (a, b, c)	Thickness
100	106.51	1.75	1.33	10.166, 10.916. 32.332	11.91
010	70.51	2.19	1.50	8.947, 16.913, 31.443	11.22
001	67.21	2.34	2.50	15.982, 15.429, 30.397	9.72
110	127.74	1.97	1.33	11.076, 11.835, 32.566	10.57
011	97.41	1.55	1.33	13.256, 14.175, 29.154	6.53
101	125.94	2.06	1.33	10.283, 12.832, 32.938	10.08
111	144.34	2.04	1.33	11.975, 12.638, 34.286	80.86

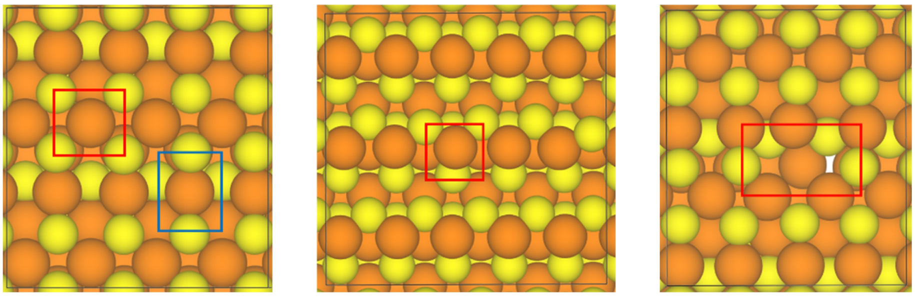

Figure 2. Left: top view of the optimized structure for the FeS (011) slab model, where the red square denotes a penta-coordinated Fe atom and the blue square the tetra-coordinated Fe atom. Central: optimized structure for the FeS (001) slab model, where the red square denotes a tri-coordinated Fe atom. Right: optimized structure for the defective FeS (001) slab model, where the red square denotes the sulphur vacancy on the surface. Colour code: yellow colour (S atoms) and orange colour (Fe atoms). The black square delimits the unit cell for each structure. Colour-coding: yellow, S atoms; orange, Fe atoms; black square, the limits of the unit cells.

Results

The proposed reaction mechanism (see Figure 1) is valid to the chosen surface active sites (i.e., Penta-Fe@FeS$_{(011)}$, Tetra-Fe@FeS$_{(011)}$, Tri-Fe@FeS$_{(001)}$ and Def-FeS$_{(011)}$). The reaction begins with the adsorption of the first H_2 molecule, followed by the adsorption of the CO molecule. We have considered that the H_2 adsorption occurs first due to its higher abundance than CO in the ISM. After the adsorption of both molecules, the first hydrogen transfer from H_2 occurs (involving the simultaneous dissociation of H_2), forming the HCO intermediate. Subsequently, the remaining H atom transfers to HCO to form H_2CO (formaldehyde). To proceed with the reaction, a second H_2 molecule is adsorbed on the surface, and the same hydrogenation steps take place, passing through first with the formation of the CH_3O intermediate and finally forming CH_3OH (methanol). The proposed reaction mechanism with the expected transition states and intermediates is depicted in Figure 3.

Reaction Mechanism on the Penta-Fe@FeS$_{(011)}$ Active Site

The stationary points and the ZPE-corrected PES for the reaction occurring on Penta-Fe@FeS$_{(011)}$ are depicted in Figure 4. The adsorption of H_2 and CO is energetically favourable (each species on different surface Fe centres), resulting in an exoergic adsorption complex of -34.43 kcal mol^{-1}. H_2 molecularly adsorbs on a pentacoordinated Fe surface atom through its H–H bond (structure C). The first H-transfer (TS$_{C\text{-}D}$) presents an intrinsic $\Delta U^{\neq}$ of 44.52 kcal mol^{-1}, leading to the endoergic formation of intermediate D. The second H-transfer (TS$_{D\text{-}E}$) has $\Delta U^{\neq} = 18.76$ kcal mol^{-1}, producing H_2CO (intermediate E) in an endoergic way with respect to intermediate D. The mechanism proceeds with the adsorption of the second H_2 molecule on a free penta-coordinated Fe surface atom, with an adsorption energy of -23.99 kcal mol^{-1} (structure F). However, at variance with the H transfers of first H_2 addition, in this second H_2 addition, the H_2 molecule needs to be dissociated first. Attempts to do a direct H transfer from the non-dissociated H_2 molecule failed. This dissociation (TS$_{F\text{-}F*}$) presents $\Delta U^{\neq}$ of 43.14 kcal mol^{-1}, leading to intermediate F*, in which the H_2 molecule is fully dissociated in a homolytic way. The third H-transfer (TS$_{F\text{-}G}$) has $\Delta U^{\neq} = 9.01$ kcal mol^{-1}, leading to the exoergic formation of CH_3O (intermediate F). The last H transfer (TS$_{G\text{-}H}$) exhibits $\Delta U^{\neq}$ of 25.39 kcal mol^{-1} in a highly exoergic step, producing finally CH_3OH.

Reaction Mechanism on the Tetra-Fe@FeS$_{(011)}$ Active Site

The stationary points and the ZPE-corrected PES for the reaction occurring on Tetra-Fe@FeS$_{(011)}$ are depicted in Figure 5. Similar to the mechanism on the Penta-Fe@FeS(011) active site, the

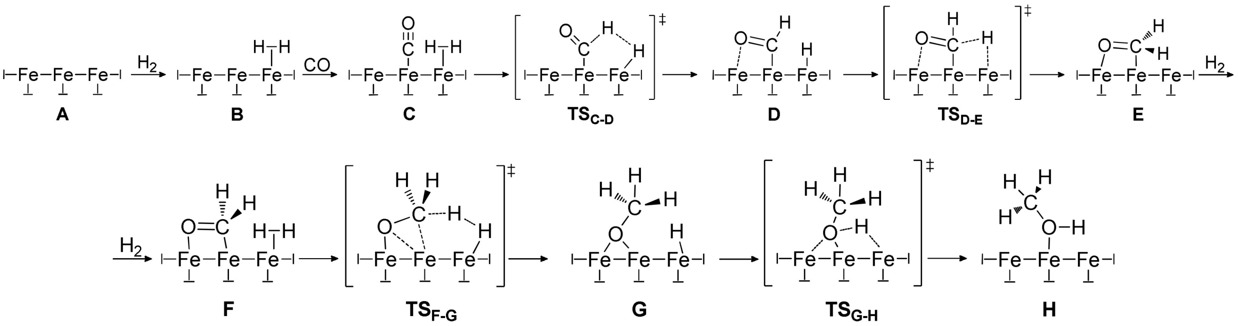

Figure 3. Proposed reaction mechanism to form methanol (CH_3OH) adopting a Fischer-Tropsch-type synthesis catalysed by FeS surfaces.

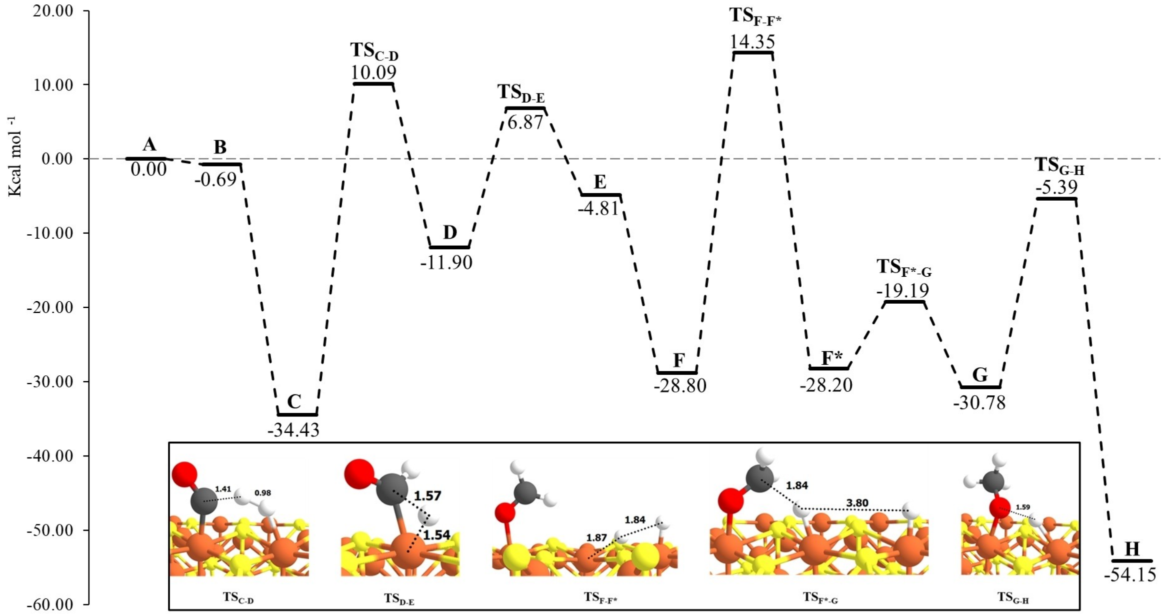

Figure 4. ZPE-corrected energy profile (in kcal mol^{-1}) for the FTT-methanol synthesis taking as the 0th energy reference the Penta-Fe@FeS$_{(011)}$ + 2H$_2$ + CO asymptote. The optimized geometries of all the transition state structures (bond distances in Å) are also shown. Colour scheme: white colour (H atoms), grey colour (C atoms), red colour (O atoms), yellow colour (S atoms) and orange colour (Fe atoms). Colour-coding: white, H atoms; grey, C atoms; red, O atoms; and orange, Fe atoms.

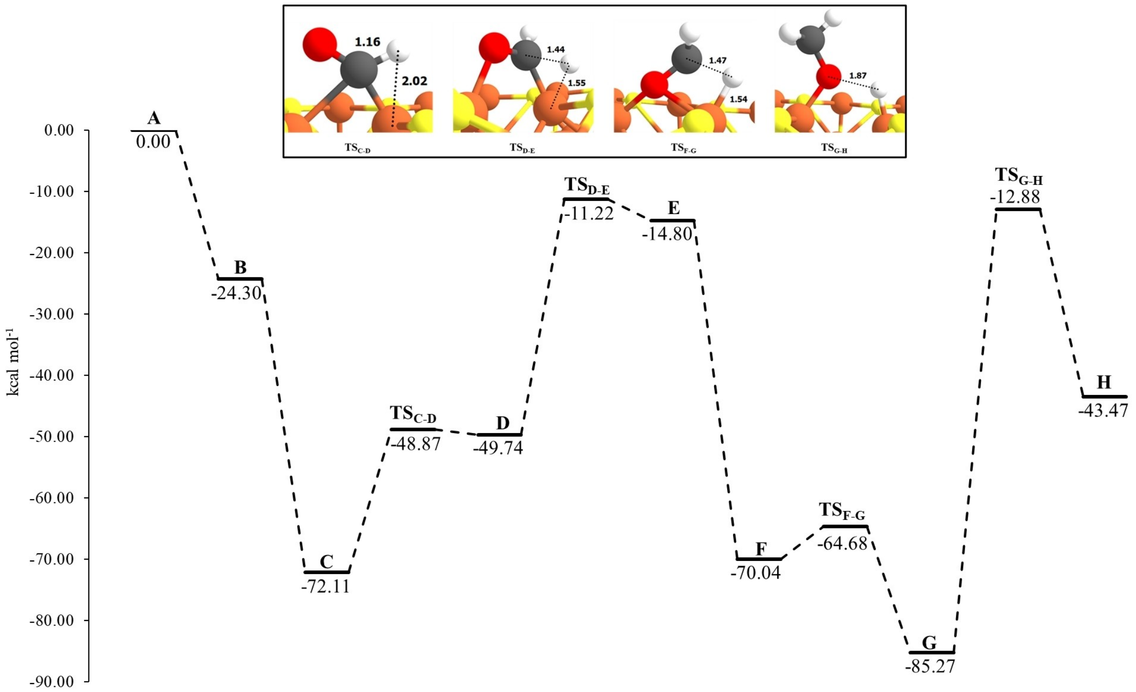

Figure 5. ZPE-corrected energy profiles (in kcal mol^{-1}) for the FTT-methanol synthesis taking as the 0th energy reference the Tetra-Fe@FeS(011) + 2H$_2$ + CO asymptote. The optimized geometries of all the transition state structures (bond distances in Å) are also shown. Colour-coding: white, H atoms; grey, C atoms; red, O atoms; and orange, Fe atoms.

adsorption of H$_2$ and CO is energetically favourable, but in this case even more, with a total adsorption energy of -72.1 kcal mol^{-1}. This is because the adsorption leads to the spontaneous dissociation of the H–H bond homolytically (structure C), resulting in a hexacoordinated Fe centre. The first H transfer (TS$_{\text{C-D}}$) has $\Delta U^{\neq} = 23.24$ kcal mol^{-1}, with an endoergic formation of HCO (intermediate D). This energy barrier is considerably lower than that on Penta-Fe@FeS$_{(011)}$ ($\Delta U^{\neq} = 44.52$ kcal mol^{-1}), indicating that the previous H–H bond cleavage facilitates the CO hydrogenation. The second H transfer (TS$_{\text{D-E}}$) exhibits a $\Delta U^{\neq}$ of 38.52 kcal mol^{-1}, forming H$_2$CO (intermediate E) in an elementary endoergic step. The adsorption of the second H_2 molecule give rise to intermediate F, with an adsorption energy of $-55.24\ kcal\,mol^{-1}$. Like the first H_2 adsorption, the spontaneous dissociation of H_2 is observed. The third H transfer (TS_{F-G}) presents an intrinsic $\Delta U^{\neq}$ as low as $5.35\ kcal\,mol^{-1}$, leading to the exoergic formation of CH_3O (intermediate G). However, due to high stability of this intermediate G, the last H transfer (TS_{G-H}) presents $\Delta U^{\neq} = 72.39\ kcal\,mol^{-1}$, giving rise to the endoergic formation of CH_3OH with respect to intermediate G.

Reaction Mechanism on the Tri-Fe@FeS$_{(001)}$ Active Site

The stationary points and the ZPE-corrected PES for the reaction occurring on Tri-Fe@FeS$_{(001)}$ are depicted in Figure 6. The adsorption of H_2 and CO forms an adsorption complex with an adsorption energy of $-81.88\ kcal\,mol^{-1}$. Here, CO adsorption induces the homolytic dissociation of H–H bond (structure C), as the first single H_2 adsorption does not gives rise to the H–H bond dissociation. The first H transfer (TS_{C-D}) presents an intrinsic $\Delta U^{\neq}$ of $35.99\ kcal\,mol^{-1}$, resulting with the endoergic formation of HCO (intermediate D). This first energy barrier is higher than that on Tetra-Fe@FeS$_{(011)}$ (where the single H_2 already dissociates upon adsorption), indicating that, while the spontaneous dissociation of H_2 facilitates CO hydrogenation, it does not consistently lead to similar energy barriers. The second H transfer (TS_{D-E}) has $\Delta U^{\neq} = 41.76\ kcal\,mol^{-1}$, forming H_2CO (intermediate E) also through an endoergic step. The adsorption of the second H_2 molecule gives rise to intermediate F, with an adsorption energy of $-25.52\ kcal\,mol^{-1}$, where H_2 dissociates in a spontaneous and homolytic way. The third H transfer (TS_{F-G}) presents $\Delta U^{\neq} = 9.69\ kcal\,mol^{-1}$, resulting with the exoergic formation of CH_3O (intermediate G). The last H transfer (TS_{G-H}) has a $\Delta U^{\neq}$ of $47.72\ kcal\,mol^{-1}$, finally producing CH_3OH in an endoergic way with respect to intermediate G.

Reaction Mechanism on the Defective Def-FeS$_{(011)}$ Active Site

The stationary points and the ZPE-corrected PES for the reaction occurring on Def-Fe@FeS$_{(011)}$ are depicted in Figure 7. The adsorption of H_2 and CO forms a favourable adsorption complex with an adsorption energy of $-80.43\ kcal\,mol^{-1}$ (structure C). Here, like on the Tri-FeS$_{(001)}$ surface active site, the CO adsorption induces the spontaneous dissociation of the H–H bond. Moreover, the adsorbed CO occupies the sulphur vacancy, being attached through its C-end to the surface. The first H transfer (TS_{C-D}) $\Delta U^{\neq} = 29.10\ kcal\,mol^{-1}$, significantly lower than that on Penta-Fe@FeS$_{(011)}$ (the non-defective analogue, with $\Delta U^{\neq} = 44.52\ kcal\,mol^{-1}$) and indicating that the vacancy favours this first step. The second H transfer (TS_{D-E}) exhibits a $\Delta U^{\neq}$ of $41.76\ kcal\,mol^{-1}$, forming H_2CO (intermediate E) in an endoergic step. The adsorption of the second H_2 molecule gives rise to intermediate F (adsorption energy of $-25.52\ kcal\,mol^{-1}$), which dissociates spontaneously H_2. The third H transfer (TS_{F-G}) has $\Delta U^{\neq} = 9.69\ kcal\,mol^{-1}$, resulting with the endoergic formation of CH_3O (intermediate G). The last H transfer (TS_{G-H}) exhibits a $\Delta U^{\neq}$ of $16.41\ kcal\,mol^{-1}$, producing CH_3OH through a final elementary endoergic step.

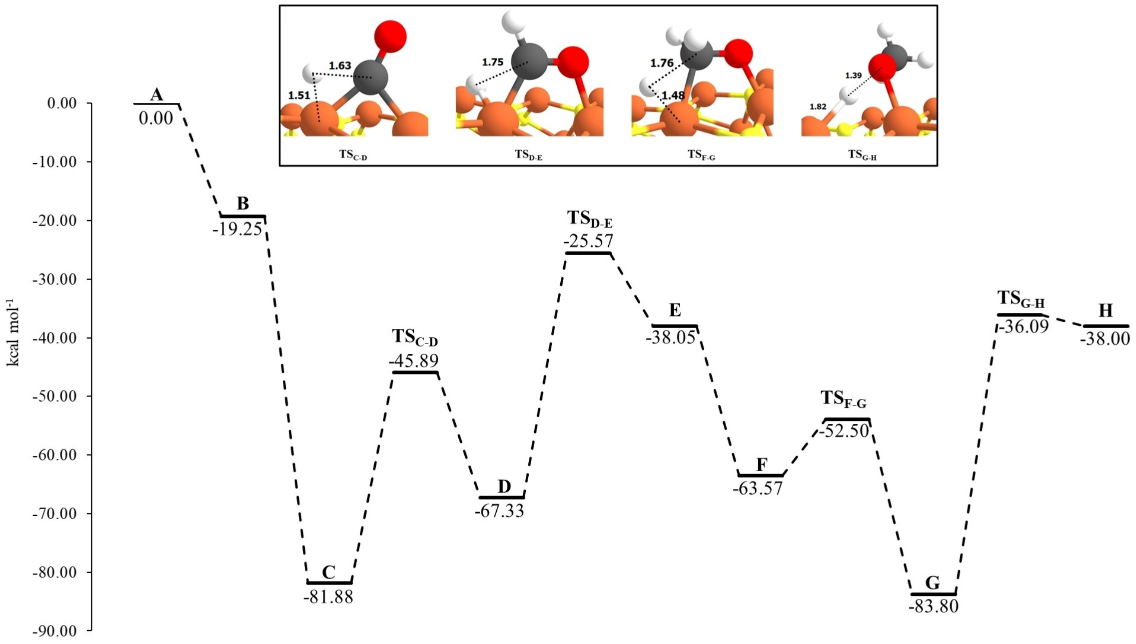

Figure 6. ZPE-corrected energy profiles (in kcal mol^{-1}) for the FTT-methanol synthesis taking as the 0th energy reference the Tri-Fe@FeS$_{(001)}$ + $2H_2$ + CO asymptote. The optimized geometries of all the transition state structures (bond distances in Å) are also shown. Colour-coding: white, H atoms; grey, C atoms; red, O atoms; and orange, Fe atoms.

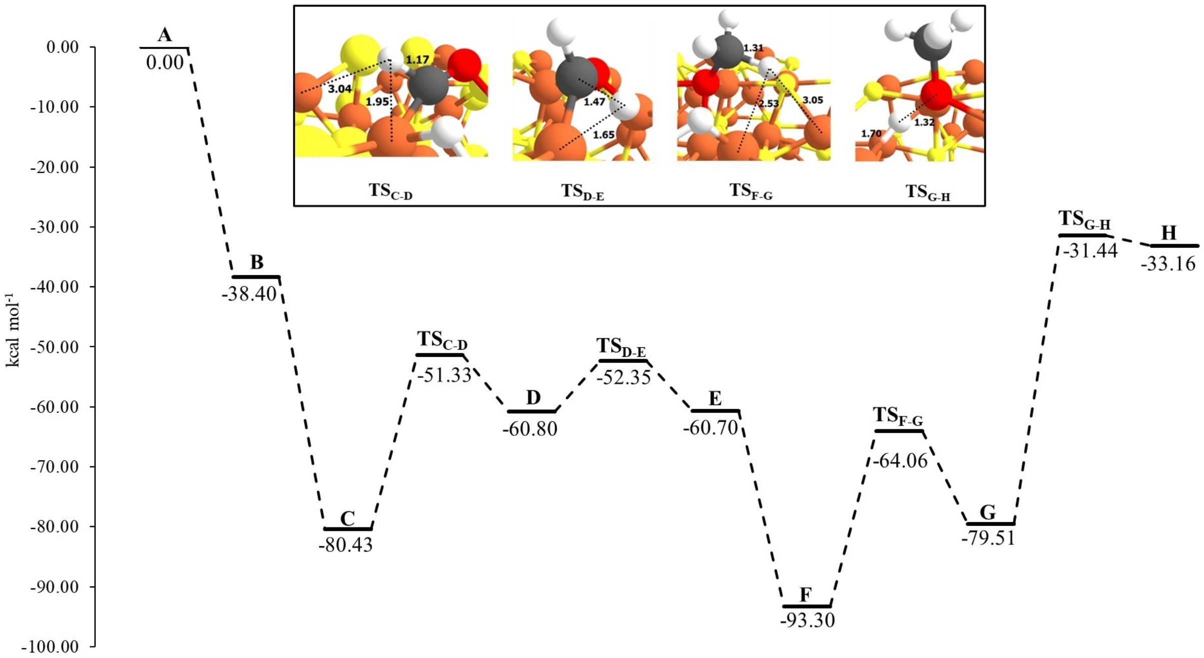

Figure 7. ZPE-corrected energy profiles (in kcal mol^{-1}) for the FTT-methanol synthesis taking as the 0th energy reference the Tri-Fe@FeS(001) + 2H_2 + CO asymptote. The optimized geometries of all the transition state structures (bond distances in Å) are also shown. Colour-coding: white, H atoms; grey, C atoms; red, O atoms; and orange, Fe atoms.

Discussion

Here, we investigated the formation of methanol via the FTT mechanism on four distinct FeS surface active sites. We considered slab models for the (011) and the (001) surfaces as, according to the calculated surface energies, they represent the most and least stable faces. The active sites are featured to have surface Fe atoms with different coordination environments (penta- and tetra-coordination in the (011) slab, and tri-coordination in the (001) slab) as well as with a sulphur vacancy in the (011) slab. Table 2 provides a comprehensive summary of the calculated $\Delta U^{\ddagger}$ values associated with the elementary steps of the FTT-CH_3OH synthesis. Table 3 provides the binding energies of CO, H_2CO and CH_3OH.

Table 2. Calculated ZPE-corrected intrinsic energy barriers (in kcal mol^{-1}) of all the elementary steps in the FTT-CH_3OH synthesis on the FeS surface active sites.

Active site	$TS_{C\text{-}D}$	$TS_{D\text{-}E}$	$TS_{F\text{-}G}$	$TS_{G\text{-}H}$
Penta-Fe@$FeS_{(011)}$	44.52	18.76	43.14^{a} / 9.01^{b}	25.39
Tetra-Fe@$FeS_{(011)}$	23.24	38.52	5.35	72.39
Tri-Fe@$FeS_{(001)}$	35.99	41.76	11.07	47.72
Def-Fe@$FeS_{(011)}$	29.10	8.45	29.24	48.07

[a] Relative energy for the transition state $TS_{F\text{-}F^*}$. [b] Relative energy for the transition state $TS_{F^*\text{-}G}$.

Table 3. Binding energies (in kcal mol^{-1}) of CO, H_2CO and H_3COH on the FeS surface active sites.

Active site	CO	H_2CO	CH_3OH
Penta-Fe@$FeS_{(011)}$	37.97	39.08	18.87
Tetra-Fe@$FeS_{(011)}$	47.83	33.52	13.47
Tri-Fe@$FeS_{(001)}$	67.74	78.07	41.85
Def-Fe@$FeS_{(011)}$	66.82	114.94	1.52

Although the mechanistic steps are almost identical in all four surface active sites, significant differences emerge regarding the elementary energy barriers and their endoergic/exoergic behaviours.

For the first H transfer, Tetra-Fe@$FeS_{(011)}$ exhibits the lowest energy barrier, while Penta-Fe@$FeS_{(011)}$ the highest one ($\Delta U^{\ddagger}$ of 23.24 and 44.52 kcal mol^{-1}, respectively, see Table 2). Notably, Penta-Fe@$FeS_{(011)}$ stands out as the only case in which H_2 does not undergo spontaneous homolytic dissociation upon adsorption, while for the remaining active sites, H_2 do spontaneously dissociate, causing a decrease of their energy barriers. However, Tri-Fe@$FeS_{(001)}$ and Def-Fe@$FeS_{(011)}$ have higher energy barriers ($\Delta U^{\ddagger}$ of 35.99 and 29.10 kcal mol^{-1}) than Tetra-Fe@$FeS_{(011)}$ ($\Delta U^{\ddagger} = 23.24$ kcal mol^{-1}). This is attributed to the coordination of the Fe centre in Tetra-Fe@$FeS_{(011)}$, as it presents hexacoordination due to the attachment of the CO molecule and the H atoms on the active site, this way stabilising the transition state on this active site.

For the second H transfer, Def-Fe@$FeS_{(011)}$ presents a ZPE-corrected energy barrier significantly smaller ($\Delta U^{\ddagger} =$ 8.45 kcal mol^{-1}) than the other surface active sites. In this case, HCO occupies the sulphur vacancy, being attached through its carbon and oxygen ends to the surface. This induces activation of the C–O bond, as evidenced by the longest C–O distance among all active sites, thereby lowering the energy barrier for its subsequent H-transfer.

Considering the third H transfer, Def-Fe@FeS$_{(011)}$ shows the highest ZPE-corrected energy barrier ($\Delta U^{\neq} = 29.24$ kcal mol-1), likely due to the stability of the H_2CO intermediate. Conversely, Penta-Fe@FeS$_{(011)}$, Tetra-Fe@FeS$_{(011)}$ and Tri-Fe@FeS$_{(001)}$ display lower ZPE-corrected energy barriers. However, on the Penta-Fe@FeS$_{(011)}$ active site, the mechanism requires a preceding step: the dissociation of the H_2 molecule, as the second H_2 molecule does not spontaneously dissociate upon adsorption and the direct H transfer from H_2 does not lead to the CH_3O formation. Such a dissociation has $\Delta U^{\neq} = 43.14$ kcal mol^{-1}, representing one of the highest energy barriers of the mechanism on this surface-active site.

Regarding the last H transfer, Tetra-Fe@FeS$_{(011)}$ presents the highest energy barrier ($\Delta U^{\neq} = 72.39$ kcal mol^{-1}) compared to the other active sites. Moreover, on Tri-Fe@FeS$_{(001)}$ and Def-Fe@FeS$_{(011)}$, this step represents that presenting the highest energy barrier along their respective FTT-CH_3OH syntheses. In contrast, for the Penta-Fe@FeS$_{(011)}$ active site, this last H-transfer presents the lowest energy barrier along the synthetic path. This is because, on Penta-Fe@FeS$_{(011)}$, the radical CH_3O intermediate is coordinated to one Fe surface atom through the oxygen, whereas for all other cases, CH_3O coordinates to two Fe surface atoms, this way stabilizing the radical. This stabilizing effect is particularly significant in Tetra-Fe@FeS$_{(011)}$ and hence its huge energy barrier.

In view of these results, it is worth highlighting that the spontaneous dissociation of the H_2 molecule upon adsorption plays a crucial role in facilitating the first and third H transfer steps by lowering their intrinsic energy barriers. This phenomenon is particularly evident in Penta-Fe@FeS$_{(011)}$, which is the only case where H_2 does not dissociate spontaneously and thus presenting the highest energy barrier amongst the different surface active sites. Also for the first and third hydrogenation steps, by comparing the other Tetra-Fe@FeS$_{(011)}$ Tri-Fe@FeS$_{(001)}$ and Def-Fe@FeS$_{(011)}$ sites, results also indicate that the active site with the higher coordination number (namely, Tetra-Fe@FeS$_{(011)}$) exhibits lower energy barriers compared to the other two active sites, which are more under-coordinated. These findings point out that under-coordinated systems may not effectively facilitate these processes. Thus, the energy barriers involving the H transfer from a dissociated H_2 depend on a delicate balance in the coordination sphere of the surface active site: high coordination implies a non-spontaneous dissociation of the adsorbed H_2 molecule (giving rise to high energy barriers, like the Penta-Fe@FeS$_{(011)}$ case), while low coordination implies an over-stabilization of the dissociated adsorption complex (and hence the high energy barriers in Tri-Fe@FeS$_{(001)}$ and Def-Fe@FeS$_{(011)}$).

For the second and fourth H transfers, the results indicate that Penta-Fe@FeS$_{(011)}$ (the more coordinated active site) presents low energy barriers, thereby facilitating these steps. In contrast, on Tetra-Fe@FeS$_{(011)}$, Tri-Fe@FeS$_{(001)}$ and Def-Fe@FeS$_{(011)}$, (more under-coordinated active sites) these steps present larger energy barriers. Accordingly, the radical HCO and CH_3O intermediates seem to be more stabilized by under-coordinated environments, challenging these H transfer steps. This finding is particularly evident for the last H-transfer on Tetra-Fe@FeS$_{(011)}$, where CH_3O is highly stabilized, hampering the step. The exception to this trend is the second H transfer on Def-Fe@FeS$_{(011)}$, as it presents the lowest energy barrier for this step amongst the surface active sites. In this case, the HCO radical occupies the sulphur vacancy of the surface, which instead of hampering the hydrogenation, the interaction activates the CO bond promoting its hydrogenation.

Finally, we present a kinetic analysis obtained from RRKM calculations. The aim is twofold: 1) assess the catalytic efficiency of the FeS surface active sites in the FTT-CH_3OH synthesis, and 2) allocate in which stages of the formation of a Solar-type planetary systems these reaction processes are feasible, considering their environmental conditions. To this end, for each surface-active site, we represented the Arrhenius plots (shown in Figure 8) considering only the step with the highest energy barrier, assuming they are the rate determining steps). The plots served to estimate at which temperature the reaction constant (k) equals to 1 year^{-1}. The choice of this reaction constant threshold is based on the fact that the half-times of interstellar molecular clouds range from 1 to 10 Myears, the rate constants thus aligning well with these astronomical timescales. Results indicate that $k = 1$ year^{-1} is only reached at $T = 543$ K, 764 K, 507 K and 608 K for the Penta-Fe@FeS$_{(011)}$, Tetra-Fe@FeS$_{(011)}$, Tri-Fe@FeS$_{(001)}$ and Def-FeS$_{(011)}$ active site respectively, which are indeed relatively high temperatures. In view of these results, the "idoneous" catalytic system is that capable to easily dissociate H_2 and keeping the formed H atoms close to CO, at the expectation that a sudden increase in temperature can trigger the reactions. The temperatures required to overcome the RSD of each process push these reaction mechanisms further in the stages of planetary system formation where higher temperatures are reached (see the astrochemical implications below).

Astrochemical Implications

FTT experiments have been conducted in laboratory settings under varying astrophysical conditions. While hydrocarbons have been successfully synthesized using dust analogues containing transition metals under conditions resembling those of a solar nebula,[47–49,73] the production of alcohols has remained challenging. Nevertheless, under conditions mimicking meteoritic materials and early Earth environments, methanol and ethanol formation have been achieved, albeit in smaller quantities compared to hydrocarbons and at temperatures around 570 K,[73] indicating that methanol formation can compete with hydrocarbon formation at these conditions. Interestingly, the identification of formaldehyde as a by-product of FTT reactions adds coherence to the overall understanding of the chemical processes involved, since formaldehyde serves as a common intermediate in the subsequent formation of both hydrocarbons and alcohols. Hence, experimental results support the notion that methanol formation could indeed occur through the proposed FTT mechanism.

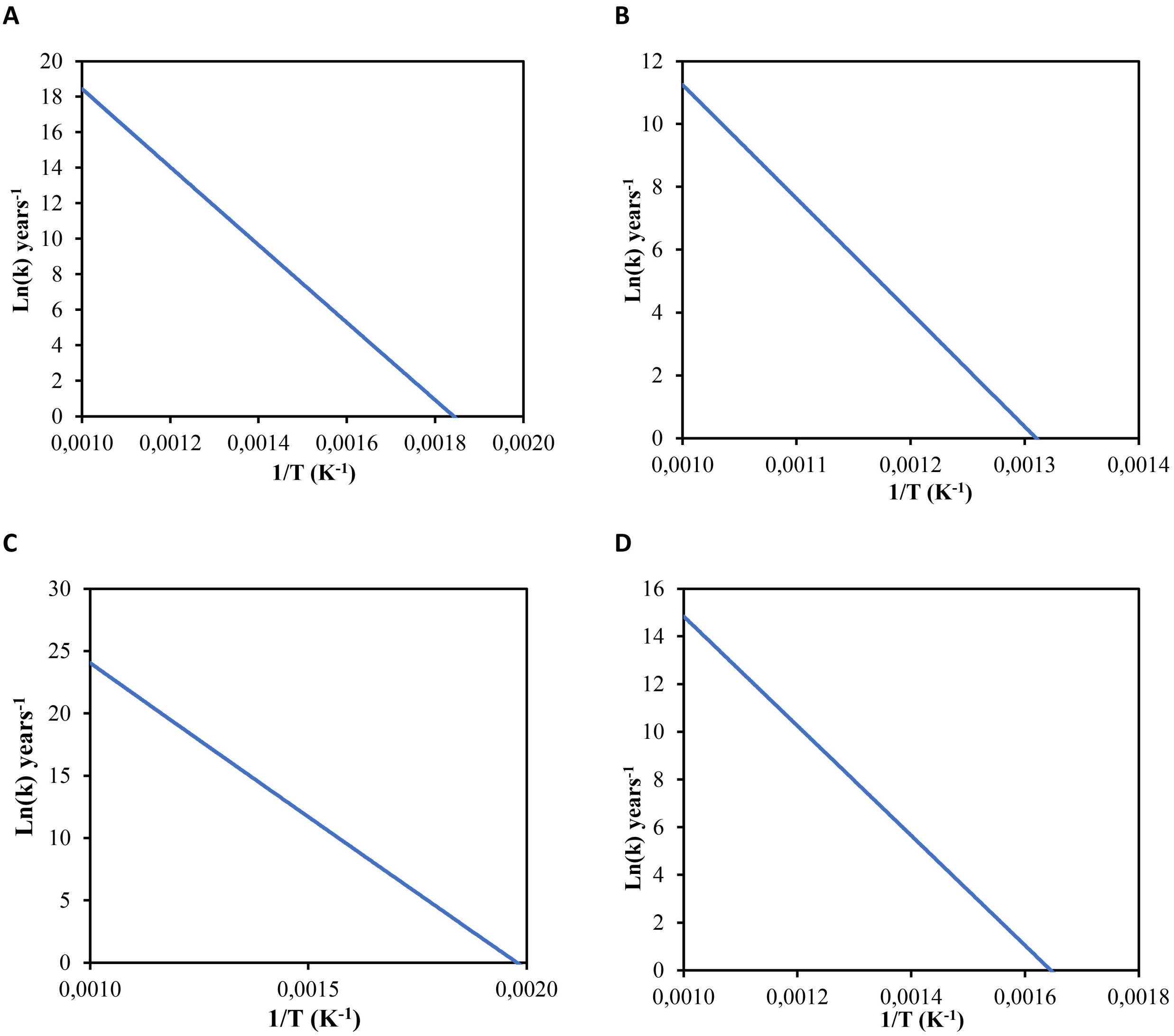

Figure 8. Arrhenius plot for the free energy barrier associated with: panel A ($TS_{C\text{-}D}$), panel B ($TS_{G\text{-}H}$), panel C ($TS_{G\text{-}H}$) and panel D ($TS_{G\text{-}H}$).

Additionally, various investigations have identified iron carbides in interplanetary dust particles,[74,75] likely originating from the carburization of iron catalysts during Fischer-Tropsch Type (FTT) processes.[76,77] Experimental studies have supported this hypothesis by demonstrating the production of Fe carbides during FTT under conditions resembling those found in solar nebulas. The presence of stable Fe carbides at high temperatures suggests catalytic carburization occurring in the solar nebula or, possibly, within protoplanetary disks.[78] Therefore, the examination of the composition and petrology of interplanetary dust particles and carbonaceous chondrite meteorites further strengthens the evidence for FTT reactions being responsible for the formation of both hydrocarbons and alcohols.

Nevertheless, FTT reactions face limitations in explaining certain aspects of meteorite composition, particularly isotopic substitution. Despite being considered as a possible mechanism for producing organic compounds in meteorites, FTT reactions struggle to accurately replicate the isotopic ratios observed in chondritic meteorites, often resulting in lighter isotopic ratios.[79,80] This discrepancy suggests that FTT reactions might not be the primary driver of volatile organic material formation in meteorites. Other processes such as ice chemistry or alterations within parental bodies may contribute more significantly to the composition of organic material in meteorites. Nonetheless, while FTT mechanism may not be the primary pathway for the organic material formation, its isotopic signatures may still be present but overshadowed by other processes.[81]

The kinetic analysis of FeS catalysis presented here suggests that FTT reactions are unlikely to occur at temperatures below ca. 500 K. Consequently, the production of methanol via FTT is not expected in cold, star-forming early regions. In dark clouds and pre-stellar cores, with temperatures of about 10 K, dust grains are covered by volatile ices, potentially shielding Fe catalytic inclusions from the surrounding gas. However, as star and planet formation progress, different environments and energy sources become available, which could facilitate FTT reactions.

In protostellar cores (with temperatures of 100–200 K), the widespread detection of methanol in the gas phase, including the expansive envelopes[82] and in shocks or outflows,[83–85] is attributed to its formation via direct atomic H addition to CO ices, followed by subsequent desorption facilitated by non-thermal mechanisms.[86,87] Nevertheless, in the central regions near the protostars, known as hot cores or hot corinos (depending on the stellar mass),[88] methanol can also undergo thermal desorption due to relatively elevated temperatures (between 100–200 K).[89–94] Thus, in these regions, where the temperatures are not conducive to FTT processes yet, the abundance of atomic H favours the addition of H to CO as the primary pathway for the formation of H_2CO and CH_3OH, thereby cancelling the significance of FTT. Nevertheless, FTT reactions may still occur in other high-temperature environments such as shocks or outflows. It is conceivable that in such regions, gas sputtering could destroy methanol in the ice, and the detected methanol might result from post-shock reactions, potentially involving FTT.[95]

Protoplanetary disks, the birthplaces of planetary systems, are known to contain a variety of chemical compounds crucial for the formation of planets. Methanol has been in particular theorized to be present in these disks, but its detection is being challenging, solely detected in one source.[96,97] Methanol is primarily observed in the disk midplane (the coldest and outer regions of the disk, spanning from tens to hundreds K), relatively close to the central star (within 100 astronomical units (AU) from the central source). This suggests that it may be released from icy grains in this region, although current astrochemical models struggle to fully explain the observed levels of methanol. These models often predict methanol abundances that significantly exceed what has been observed by several orders of magnitude.[98] Consequently, even sophisticated models overlook a potential source of methanol in the innermost regions of protoplanetary disks, likely attributable to Fischer-Tropsch-Type (FTT) processes under the conditions prevailing in the inner disk.

Methanol has been identified in comets,[99–103] likely originating from earlier phases of planetary development, including the ices of primitive dust grains.[104] Consequently, the abundance of methanol is expected to vary depending on the protoplanetary region from which it originated, as well as the environmental conditions it encountered during its evolution. These conditions include the temperatures of the protostellar gas and protoplanetary disk, the level of CO depletion in primordial volatile gases,[105] and the irradiation conditions.[106] Although there is no direct evidence supporting the occurrence of FTT reactions during the lifespan of comets, some of the organic compounds found in comets may have been produced through FTT reactions on the surfaces of grains in specific regions of the solar nebula.[107] For instance, the presence of ethylene in cometary comas, the origin of which remains uncertain,[108] could potentially be linked to such processes.

FTT reactions may indeed play a role in the latter stages of planetary development, such as in the primitive atmospheres of terrestrial planets or their moons. Proto-Earth-sized protoplanets have the capacity to efficiently accumulate H_2 from the protoplanetary nebula,[109,110] which is also abundant in CO. In these settings, the presence of potentially catalytic Fe-containing inclusions, possibly delivered through chondritic material, combined with increasing temperatures in planetary atmospheres, creates an ideal environment for FTT reactions. As a result, alcohols like CH_3OH and hydrocarbons can be generated.[111]

Conclusions

In this work, we present a comprehensive computational study to investigate the catalytic properties of cosmic FeS to synthesize CH_3OH via Fischer-Tropsch-type (FTT) processes from the reactivity between CO and two H_2 molecules. The stoichiometric FeS troilite form has been chosen as cosmic iron sulphide material since it has been identified forming part of inclusions in pre-solar bodies like meteorites, comets, and interplanetary dust particles. Different slab surface models have been generated, with the surface energies indicating that the (011) surface is the most stable and the (001) surface is the least stable. These two slabs have been selected to study the proposed FTT reactions because they exhibit a variety of coordination environments for the Fe centres on the surface, i.e., tetra- and penta-coordination in the (011) and tri-coordination in the (001). Moreover, a defective (011) slab model with a S vacancy at its surface has also been considered to assess any catalytic enhancement due to the presence of such a point defect.

The studied reaction mechanisms show differences depending on the slab model and the coordination environment of the Fe centre. The main differences between the four systems are, first, the occurrence (or not) of the spontaneous dissociation of the H_2 molecules upon adsorption. A clear example is the penta-coordinated structure, where the first H_2 atoms adsorbs in a molecular way, which consequently presents a high energy barrier for the first hydrogenation of CO. This behaviour is completely different for the tetra-coordinated system, where the first barrier is relatively small because the H_2 molecule dissociates upon adsorption. Another difference observed between the FeS surfaces is the energy barriers for the hydrogenation of the radical (HCO and CH_3O) intermediates. On the tetra-coordinated and tri-coordinated systems, due to the low coordination number of the Fe centres, these intermediates are highly stabilized on the surfaces, giving rise to high energy barriers in their hydrogenation. Finally, the defective system is apparently the system presenting the best catalytic properties, at least for the first three steps. However, the CH_3O intermediate is highly stabilized on the surface because the oxygen atom falls within the S vacancy, and hence the high energy barrier with respect to the final CH_3OH formation.

To further comprehend the catalytic activity of the FeS surfaces and determine the conditions and regions where the reaction processes are feasible within an astrochemistry framework, kinetic calculations have been performed. From the kinetic data, we observe that, although the rate determining steps of the different systems concern different steps of the FTT reaction mechanism, all of them require temperatures above the 500 K to be fast in astronomical timescales (i.e., $k = 1\ \text{year}^{-1}$). This data affirms that the FTT-CH_3OH formation can only happen in the later, evolved stages of the formation of planetary systems, where such a high temperature can be reached. Despite this, present results point out cosmic FeS material as a versatile astrocatalytic system beyond the formation of methanol. Indeed, the FeS catalytic properties shown in this work can be extended to other chemical processes, thereby setting a link between the rich chemistry present in meteorites and interplanetary dust particles with FeS inclusions. This link may be crucial in cosmic chemical evolution and ultimately in the emergence of life in primitive Earth.

Results of the present work evidence the occurrence of true astrocatalysis, introducing a novel spectrum of synthetic routes and opening avenues for further exploration into the role of cosmic grains as heterogeneous catalysts that can contribute to the chemical evolution in the Universe.

Acknowledgements

This project has received funding within the European Union's Horizon 2020 research and innovation program from the European Research Council (ERC) for the project "Quantum Chemistry on Interstellar Grains" (QUANTUMGRAIN), grant agreement no. 865657. G.P. thankfully acknowledges financial support by the Spanish Ministry of Universities and the European Union's Next Generation EU fund for a Margarita Salas contract. MICINN is also acknowledged for funding the project PID2021-126427NB-I00 and CNS2023-144902. The authors thankfully acknowledge RES resources provided by Univ. Valencia for the use of Tirant (activity QHS-2022-2-0022) and by BSC for the use of MareNostrum (activity QHS-2023-1-0019). The supercomputational facilities provided by CSUC are also acknowledged. The EuroHPC Joint Undertaking through the Regular Access call project no. 2023R01-112, hosted by the Ministry of Education, Youth and Sports of the Czech Republic through the e-INFRA CZ (ID: 90254) is also acknowledged.

Conflict of Interests

The authors declare no conflict of interest.

Data Availability Statement

The data that support the findings of this study are openly available in Zenodo at https://doi.org/10.5281/zenodo.10805870, reference number 10805870.

Keywords: Density functional calculations · Astrochemistry · Surface modelling · Heterogeneous catalysis · Reactions kinetics

[1] P. Caselli, C. Ceccarelli, *Astron. Astrophys. Rev.* **2012**, *20*, 1–68.
[2] S. Kwok, *Astron. Astrophys. Rev.* **2016**, *24*, 1–27.
[3] B. A. McGuire, *Astrophys. J. Suppl. Ser.* **2022**, *259*, 30.
[4] L. E. Snyder, D. Buhl, B. Zuckerman, P. Palmer, *Phys. Rev. Lett.* **1969**, *22*, 679–681.
[5] P. Caselli, F. F. S. Van Der Tak, C. Ceccarelli, A. Bacmann, *Astron. Astrophys.* **2003**, *403*, 37–41.
[6] S. Cazaux, A. G. G. M. Tielens, C. Ceccarelli, A. Castets, V. Wakelam, E. Caux, B. Parise, D. Teyssier, *Astrophys. J.* **2003**, *593*, L51–L55.
[7] E. Herbst, E. F. Van Dishoeck, *Annu. Rev. Astron. Astrophys.* **2009**, *47*, 427–480.
[8] E. Herbst, *Int. Rev. Phys. Chem.* **2017**, *36*, 287–331.
[9] C. Ceccarelli, P. Caselli, F. Fontani, R. Neri, A. López-Sepulcre, C. Codella, S. Feng, I. Jiménez-Serra, B. Lefloch, J. E. Pineda, C. Vastel, F. Alves, R. Bachiller, N. Balucani, E. Bianchi, L. Bizzocchi, S. Bottinelli, E. Caux, A. Chacón-Tanarro, et al., *Astrophys. J.* **2017**, *850*, 176.
[10] R. Saladino, G. Botta, S. Pino, G. Costanzo, E. Di Mauro, *Chem. Soc. Rev.* **2012**, *41*, 5526–5565.
[11] C. Ceccarelli, *Faraday Discuss.* **2023**, *245*, 11–51.
[12] J. Enrique-Romero, A. Rimola, C. Ceccarelli, P. Ugliengo, N. Balucani, D. Skouteris, *Astrophys. J. Suppl. Ser.* **2022**, *259*, 39.
[13] S. Pizzarello, *Acc. Chem. Res.* **2006**, *39*, 231–237.
[14] K. Altwegg, H. Balsiger, A. Bar-Nun, J. J. Berthelier, A. Bieler, P. Bochsler, C. Briois, U. Calmonte, M. R. Combi, H. Cottin, J. De Keyser, F. Dhooghe, B. Fiethe, S. A. Fuselier, S. Gasc, T. I. Gombosi, K. C. Hansen, M. Haessig, A. Jäckel, et al., *Sci. Adv.* **2016**, *2*, e1600285.
[15] S. A. Sandford, J. Aléon, C. M. O. D. Alexander, T. Araki, S. Bajt, G. A. Baratta, J. Borg, J. P. Bradley, D. E. Brownlee, J. R. Brucato, M. J. Burchell, H. Busemann, A. Butterworth, S. J. Clemett, G. Cody, L. Colangeli, G. Cooper, L. D'Hendecourt, Z. Djouadi, et al., *Science* **2006**, *314*, 1720–1724.
[16] A. Rimola, N. Balucani, C. Ceccarelli, P. Ugliengo, *Int. J. Mol. Sci.* **2022**, *23*, 4252.
[17] A. I. Vasyunin, E. Herbst, *Astrophys. J.* **2013**, *769*, 34.
[18] N. Balucani, C. Ceccarelli, V. Taquet, *Mon. Not. R. Astron. Soc. Lett.* **2015**, *449*, L16–L20.
[19] R. T. Garrod, E. Herbst, *Astron. Astrophys.* **2006**, *457*, 927–936.
[20] R. T. Garrod, S. L. W. Weaver, E. Herbst, *Astrophys. J.* **2008**, *682*, 283–302.
[21] J. K. Jørgensen, A. Belloche, R. T. Garrod, *Annu. Rev. Astron. Astrophys.* **2020**, *58*, 727–778.
[22] M. Jin, R. T. Garrod, *Astrophys. J. Suppl. Ser.* **2020**, *249*, 26.
[23] V. Wakelam, E. Bron, S. Cazaux, F. Dulieu, C. Gry, P. Guillard, E. Habart, L. Hornekær, S. Morisset, G. Nyman, V. Pirronello, S. D. Price, V. Valdivia, G. Vidali, N. Watanabe, *Mol. Astrophys.* **2017**, *9*, 1–36.
[24] D. Hollenbach, E. E. Salpeter, *J. Chem. Phys.* **1970**, *53*, 79–86.
[25] D. Hollenbach, E. E. Salpeter, *Astrophys. J.* **1971**, *163*, 155.
[26] G. Vidali, *Chem. Rev.* **2013**, *113*, 8762–8782.
[27] H. C. van de Hulst, *The Solid Particles of Interstellar Space. A Source Book in Astronomy and Astrophysics.* Harvard University Press, 1979.
[28] R. Smoluchowski, *J. Phys. Chem.* **1983**, *87*, 4229–4233.
[29] B. A. Sargent, W. J. Forrest, C. Tayrien, M. K. McClure, A. Li, A. R. Basu, P. Manoj, D. M. Watson, C. J. Bohac, E. Furlan, K. H. Kim, J. D. Green, G. C. Sloan, *Astrophys. J.* **2009**, *690*, 1193–1207.
[30] L. P. Keller, S. Hony, J. P. Bradley, F. J. Molster, L. B. F. M. Waters, J. Bouwman, A. De Kotert, D. E. Brownlee, G. J. Flynn, T. Henning, H. Mutschke, *Nature* **2002**, *417*, 148–150.
[31] W. W. Duley, *Astrophys. J.* **2000**, *528*, 841–848.
[32] K. Lodders, B. Fegley, *Geochem.* **2023**, *83*, 1220–1247.
[33] S. Sasaki, K. Nakamura, Y. Hamabe, E. Kurahashi, T. Hiroi, *Nature* **2001**, *410*, 555–557.
[34] J. A. Nuth III, S. B. Charnley, N. M. Johnson, *Meteorites Early Sol. Syst. II* **2006**, *147*, 147–167.
[35] A. P. Jones, *J. Geophys. Res. [Space Phys.]* **2000**, *105*, 10257–10268.
[36] E. B. Jenkins, *Astrophys. J.* **2009**, *700*, 1299–1348.
[37] B. D. Savage, R. C. Bohlin, *Astrophys. J.* **1979**, *229*, 136.
[38] E. Costantini, M. J. Freyberg, P. Predehl, *Astron. Astrophys.* **2005**, *444*, 187–200.
[39] M. Min, L. B. F. M. Waters, A. De Koter, J. W. Hovenier, L. P. Keller, F. Markwick-Kemper, *Astron. Astrophys.* **2007**, *462*, 667–676.
[40] J. Xiang, J. C. Lee, M. A. Nowak, J. Wilms, *Astrophys. J.* **2011**, *738*, 78.
[41] A. P. Jones, L. Fanciullo, M. Köhler, L. Verstraete, V. Guillet, M. Bocchio, N. Ysard, *Astron. Astrophys.* **2013**, *558*, A62.
[42] L. P. Keller, S. Hony, J. P. Bradley, F. J. Molster, L. B. F. M. Waters, J. Bouwman, A. De Kotert, D. E. Brownlee, G. J. Flynn, T. Henning, H. Mutschke, *Nature* **2002**, *417*, 148–150.
[43] Z. R. Dai, J. P. Bradley, *Geochim. Cosmochim. Acta* **2001**, *65*, 3601–3612.

[44] M. E. Palumbo, T. R. Geballe, A. G. G. M. Tielens, *Astrophys. J.* **1997**, *479*, 839–844.
[45] T. Matsumoto, D. Harries, F. Langenhorst, A. Miyake, T. Noguchi, *Nat. Commun.* **2020**, *11*, 1–8.
[46] J. P. Bradley, *Science* **1994**, *265*, 925–929.
[47] R. F. Ferrante, M. H. Moore, J. A. Nuth, T. Smith, *Icarus* **2000**, *145*, 297–300.
[48] Y. Sekine, S. Sugita, T. Shido, T. Yamamoto, Y. Iwasawa, T. Kadono, T. Matsui, *Meteorit. Planet. Sci.* **2006**, *41*, 715–729.
[49] J. Llorca, I. Casanova, *Meteorit. Planet. Sci.* **1998**, *33*, 243–251.
[50] V. Cabedo, J. Llorca, J. M. Trigo-Rodriguez, A. Rimola, *Astron. Astrophys.* **2021**, *650*, A160.
[51] G. Pareras, V. Cabedo, M. McCoustra, A. Rimola, *Astron. Astrophys.* **2023**, *680*, A57.
[52] M. Ferusa, D. Nesvorný, J. Šponer, P. Kubelík, R. Michacíková, V. Shestivská, J. E. Šponer, S. Civiš, *Proc. Natl. Acad. Sci. USA.* **2015**, *112*, 657–662.
[53] R. Saladino, E. Carota, G. Botta, M. Kapralov, G. N. Timoshenko, A. Y. Rozanov, E. Krasavin, E. Di Mauro, *Proc. Natl. Acad. Sci. USA* **2015**, *112*, E2746–E2755.
[54] R. Saladino, G. Botta, M. Delfino, E. Di Mauro, *Chem. A Eur. J.* **2013**, *19*, 16916–16922.
[55] L. Rotelli, J. M. Trigo-Rodríguez, C. E. Moyano-Cambero, E. Carota, L. Botta, E. Di Mauro, R. Saladino, *Sci. Rep.* **2016**, *6*, 1–7.
[56] J. Hutter, M. Iannuzzi, F. Schiffmann, J. Vandevondele, *Wiley Interdiscip. Rev.: Comput. Mol. Sci.* **2014**, *4*, 15–25.
[57] J. P. Perdew, A. Ruzsinszky, G. I. Csonka, O. A. Vydrov, G. E. Scuseria, L. A. Constantin, X. Zhou, K. Burke, *Phys. Rev. Lett.* **2008**, *100*, 136406.
[58] S. Grimme, J. Antony, S. Ehrlich, H. Krieg, *J. Chem. Phys.* **2010**, *132*, 154104.
[59] J. Hutter, M. Iannuzzi, F. Schiffmann, J. Vandevondele, *Wiley Interdiscip. Rev.: Comput. Mol. Sci.* **2014**, *4*, 15–25.
[60] J. Vandevondele, M. Krack, F. Mohamed, M. Parrinello, T. Chassaing, J. Hutter, *Comput. Phys. Commun.* **2005**, *167*, 103–128.
[61] S. Goedecker, M. Teter, *Phys. Rev. B: Condens. Matter Mater. Phys.* **1996**, *54*, 1703–1710.
[62] G. Lippert, J. Hutter, M. Parrinello, *Mol. Phys.* **1997**, *92*, 477–488.
[63] A. D. Becke, *J. Chem. Phys.* **1993**, *98*, 1372–1377.
[64] C. Lee, W. Yang, R. G. Parr, *Phys. Rev. B* **1988**, *37*, 785–789.
[65] M. Guidon, J. Hutter, J. VandeVondele, *J. Chem. Theory Comput.* **2009**, *5*, 3010–3021.
[66] M. Guidon, J. Hutter, J. Vandevondele, *J. Chem. Theory Comput.* **2010**, *6*, 2348–2364.
[67] R. A. Marcus, *J. Chem. Phys.* **1952**, *20*, 359–364.
[68] J. Enrique-Romero, A. Rimola, **2024**, doi: 10.5281/ZENODO.10518616.
[69] C. Eckart, *Phys. Rev.* **1930**, *35*, 1303–1309.
[70] T. Lamberts, P. K. Samanta, A. Köhn, J. Kästner, *Phys. Chem. Chem. Phys.* **2016**, *18*, 33021–33030.
[71] E. Mates-Torres, A. Rimola, *J. Appl. Crystallogr.* **2024**, *57*, 503–508.
[72] C. Stampfl, A. Soon, S. Piccinin, H. Shi, H. Zhang, *J. Phys. Condens. Matter* **2008**, *20*, 184021.
[73] V. Cabedo, J. Llorca, J. M. Trigo-Rodriguez, A. Rimola, *Astron. Astrophys.* **2021**, *650*, A160.
[74] I. D. R. Mackinnon, F. J. M. Rietmeijer, *Rev. Geophys.* **1987**, *25*, 1527–1553.
[75] J. P. Bradley, D. E. Brownlee, P. Fraundorf, *Science* **1984**, *223*, 56–58.
[76] J. A. Amelse, J. B. Butt, L. H. Schwartz, *J. Phys. Chem.* **1978**, *82*, 558–563.
[77] E. E. Unmuth, L. H. Schwartz, J. B. Butt, *J. Catal.* **1980**, *63*, 404–414.
[78] A. J. Brearley, *Meteorit. Planet. Sci.* **2021**, *56*, 108–126.
[79] N. M. Johnson, J. E. Elsila, M. Kopstein, J. A. Nuth, *Meteorit. Planet. Sci.* **2012**, *47*, 1029–1034.
[80] J. R. Cronin, S. Pizzarello, *Geochim. Cosmochim. Acta* **1990**, *54*, 2859–2868.
[81] C. M. O. D. Alexander, G. D. Cody, B. T. De Gregorio, L. R. Nittler, R. M. Stroud, *Chem. Erde* **2017**, *77*, 227–256.
[82] L. E. Kristensen, E. F. Van Dishoeck, T. A. Van Kempen, H. M. Cuppen, C. Brinch, J. K. Jørgensen, M. R. Hogerheijde, *Astron. Astrophys.* **2010**, *516*, A57.
[83] R. Bachiller, S. Liechti, C. M. Walmsley, F. Colomer, *Astron. Astrophys.* **1995**, *295*, L51.
[84] R. Bachiller, M. Pérez Gutiérrez, *Astrophys. J.* **1997**, *487*, L93–L96.
[85] J. Holdship, S. Viti, C. Codella, J. Rawlings, I. Jimenez-Serra, Y. Ayalew, J. Curtis, A. Habib, J. Lawrence, S. Warsame, S. Horn, *Astrophys. J.* **2019**, *880*, 138.
[86] G. W. Fuchs, H. M. Cuppen, S. Ioppolo, C. Romanzin, S. E. Bisschop, S. Andersson, E. F. Van Dishoeck, H. Linnartz, *Astron. Astrophys.* **2009**, *505*, 629–639.
[87] N. Watanabe, A. Kouchi, *Astrophys. J.* **2002**, *571*, L173–L176.
[88] P. Nazari, M. L. Van Gelder, E. F. Van Dishoeck, B. Tabone, M. L. R. Van 'T Hoff, N. F. W. Ligterink, H. Beuther, A. C. A. Boogert, A. Caratti O Garatti, P. D. Klaassen, H. Linnartz, V. Taquet, Tychoniec, *Astron. Astrophys.* **2021**, *650*, A150.
[89] E. F. van Dishoeck, G. A. Blake, D. J. Jansen, T. D. Groesbeck, *Astrophys. J.* **1995**, *447*, 760.
[90] F. F. S. Van Der Tak, *Astron. Astrophys.* **2000**, *361*, 327–339.
[91] C. Ceccarelli, *Astron. Astrophys.* **2000**, *362*, 1122–1126.
[92] F. L. Schöier, J. K. Jørgensen, E. F. Van Dishoeck, G. A. Blake, *Astron. Astrophys.* **2002**, *390*, 1001–1021.
[93] S. Maret, C. Ceccarelli, A. G. G. M. Tielens, E. Caux, B. Lefloch, A. Faure, A. Castets, D. R. Flower, *Astron. Astrophys.* **2005**, *442*, 527–538.
[94] J. K. Jorgensen, T. L. Bourke, P. C. Myers, F. L. Schoier, E. F. van Dishoeck, D. J. Wilner, *Astrophys. J.* **2005**, *632*, 973–981.
[95] A. N. Suutarinen, L. E. Kristensen, J. C. Mottram, H. J. Fraser, E. F. Van Dishoeck, *Mon. Not. R. Astron. Soc.* **2014**, *440*, 1844–1855.
[96] C. Walsh, R. A. Loomis, K. I. Öberg, M. Kama, M. L. R. van 't Hoff, T. J. Millar, Y. Aikawa, E. Herbst, S. L. Widicus Weaver, H. Nomura, *Astrophys. J.* **2016**, *823*, L10.
[97] L. Podio, F. Bacciotti, D. Fedele, C. Favre, C. Codella, K. L. J. Rygl, I. Kamp, G. Guidi, E. Bianchi, C. Ceccarelli, D. Coffey, A. Garufi, L. Testi, *Astron. Astrophys.* **2019**, *623*, L6.
[98] C. Walsh, S. Vissapragada, H. McGee, *Proc. Int. Astron. Union* **2017**, *13*, 395–402.
[99] S. Hoban, M. Mumma, D. C. Reuter, M. DiSanti, R. R. Joyce, A. Storrs, *Icarus* **1991**, *93*, 122–134.
[100] D. C. Reuter, *Astrophys. J.* **1992**, *386*, 330.
[101] J. K. Davies, M. J. Mumma, D. C. Reuter, S. Hoban, H. A. Weaver, P. J. Puxley, S. L. Lumsden, *Mon. Not. R. Astron. Soc.* **1993**, *265*, 1022–1026.
[102] P. Eberhardt', R. Meier, D. Krankowsky, R. R. Hodges, *Astron. Astrophys.* **1994**, *288*, 315–329.
[103] L. Le Roy, K. Altwegg, H. Balsiger, J. J. Berthelier, A. Bieler, C. Briois, U. Calmonte, M. R. Combi, J. De Keyser, F. Dhooghe, B. Fiethe, S. A. Fuselier, S. Gasc, T. I. Gombosi, M. Hassig, A. Jackel, M. Rubin, C. Y. Tzou, *Astron. Astrophys.* **2015**, *583*, A1.
[104] M. Rubin, K. Altwegg, H. Balsiger, J. J. Berthelier, M. R. Combi, J. de Keyser, M. Drozdovskaya, B. Fiethe, S. A. Fuselier, S. Gasc, T. I. Gombosi, N. Hänni, K. C. Hansen, U. Mall, H. Rème, I. R. H. G. Schroeder, M. Schuhmann, T. Sémon, J. H. Waite, et al., *Mon. Not. R. Astron. Soc.* **2019**, *489*, 594–607.
[105] S. Faggi, M. Lippi, M. J. Mumma, G. L. Villanueva, *Planet. Sci. J.* **2023**, *4*, 8.
[106] R. L. Hudson, M. H. Moore, *Icarus* **1999**, *140*, 451–461.
[107] J. Llorca, *Adv. Sp. Res.* **2002**, *30*, 1469–1472.
[108] E. Dartois, *Mon. Not. R. Astron. Soc.* **2021**, *504*, 4369–4376.
[109] A. Stökl, E. A. Dorfi, C. P. Johnstone, H. Lammer, *Astrophys. J.* **2016**, *825*, 86.
[110] H. Lammer, A. L. Zerkle, S. Gebauer, N. Tosi, L. Noack, M. Scherf, E. Pilat-Lohinger, M. Güdel, J. L. Grenfell, M. Godolt, A. Nikolaou, *Astron. Astrophys. Rev.* **2018**, *26*, 1–72.
[111] M. E. Kress, C. P. McKay, *Icarus* **2004**, *168*, 475–483.

Manuscript received: March 11, 2024
Revised manuscript received: May 27, 2024
Accepted manuscript online: May 28, 2024
Version of record online: July 12, 2024